

## NANOINDENTATION OF TRABECULAR BONE – COMPARISON WITH UNIAXIAL TESTING OF SINGLE TRABECULA

ONDŘEJ JIROUŠEK<sup>a\*</sup>, JIŘÍ NĚMEČEK<sup>b</sup>,  
DANIEL KYTÝŘ<sup>a</sup>, JIŘÍ KUNECKÝ<sup>a</sup>, PETR  
ZLÁMAL<sup>a</sup>, and TOMÁŠ DOKTOR<sup>a</sup>

<sup>a</sup> Institute of Theoretical and Applied Mechanics, Academy of Sciences of the Czech Republic, v.v.i., Prosecká 76, 190 00 Prague 9, <sup>b</sup> Czech Technical University in Prague, Faculty of Civil Engineering, Thákurova 7/2077, 166 29 Prague 6, Czech Republic  
jirousek@itam.cas.cz

Keywords: trabecular bone, nanoindentation, micromechanics, constitutive modelling

### 1. Introduction

Knowledge of deformation behaviour of trabecular bone in response to mechanical loading is important for better understanding of the relationship between the microstructure and overall mechanical properties. Due to the increased computational power and powerful imaging techniques it is possible to perform numerical simulations with microstructural finite element (FE) models reflecting the true microstructure of the complex material<sup>1</sup>. Information about the microstructure can be obtained using the microfocus computed tomography (micro-CT). The deformation behaviour can be captured applying the micro-CT technique to a sample under gradual loading<sup>2</sup>.

For the microstructural FE models it is necessary to measure the material properties at the level of single trabecula. One of the established methods for evaluation of the material properties at this level is nanoindentation<sup>3</sup>. It has been confirmed by several authors that valid microstructural models of trabecular bone can be built using high-resolution micro-CT models and material properties from nanoindentation under wet conditions<sup>4</sup>. The agreement between experiments and micro-FE models has already been published, however, results of experimental investigation using standard mechanical testing of single trabeculae remains scattered. One of the reasons for the high discrepancy in experimental results can be attributed to improper boundary conditions; second reason is difficult precise measurement of the strains. In this study a comparison between the mechanical properties assessed by nanoindentation and properties obtained from tension tests of extracted trabeculae is performed.

### 2. Materials and Methods

#### Single trabecula tensile tests

Small blocks of trabecular bone were extracted from proximal human femur (male, 72 years). The blocks were cleaned of marrow and grease in a nonionic detergent in an

ultrasonic cleaner at a temperature not exceeding 37 °C. The cleaning was repetitive not to exceed the temperature limit. The sample was then dried at room temperature. Long straight trabeculae were identified in these blocks under a magnifying glass (4× magnification). The trabeculae were carefully extracted using a sharp-tip scalpel. The ends of the trabeculae were dipped in a two-component glue (UHUplus schnellfest 2-K-Epoxidharzkleber, UHU GmbH & Co. KG, Baden, Germany) and stored for 48h at room temperature. The drops of glue at the trabecula ends were used for manipulation with the sample using a pair of tweezers.

The manipulation droplets of glue were used to attach the sample to the end-plates of a laboratory uniaxial tension-compression device specially designed for these experiments. Fast-setting glue (Loctite Super Attak Ultra Plastik, Henkel Ireland Ltd., Ireland) was used for this purpose and the glue was allowed to set for 2 hours prior the experiment at room temperature.

Tension-compression of the sample was provided by means of a precision linear stage M-UMR3.5 with differential micrometer DM11-5 (Newport Corp., USA, sensitivity 0.1 µm, travel range 5 mm) while manipulation (centering) of the fixed end was provided by Y-Z translational stage (Standa Ltd., Lithuania, sensitivity 1 µm, travel range 25 mm). The load was measured using a small-scale load cell FBB350 (FUTEK Advanced Sensor Technology, Inc., USA, load capacity 4.5 N) attached to the Y-Z translational stage.

The samples were tested in displacement-controlled uniaxial tension tests. The load was applied by moving the precision linear stage away from the fixed end of the sample. The whole experiment was captured using a high-resolution CCD camera (VDS Vosskuhler GmbH, Germany) attached to optical microscope (Navitar Imaging Inc., USA). The camera is attached to a PC by firewire cable enabling to capture 15 images per second with 24× magnification.

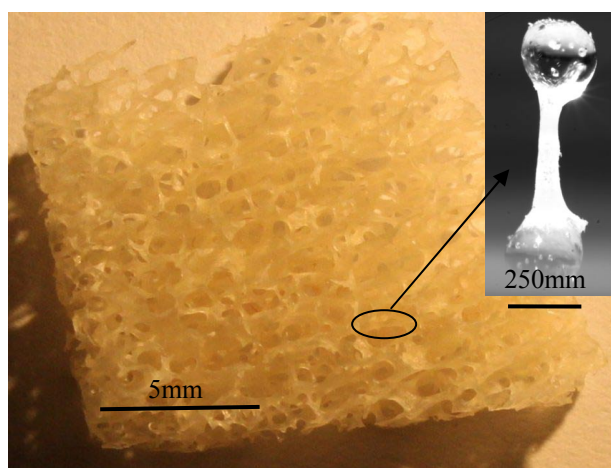


Fig. 1. A block of trabecular bone after cleaning. Extracted trabecula with droplets of glue covering the ends

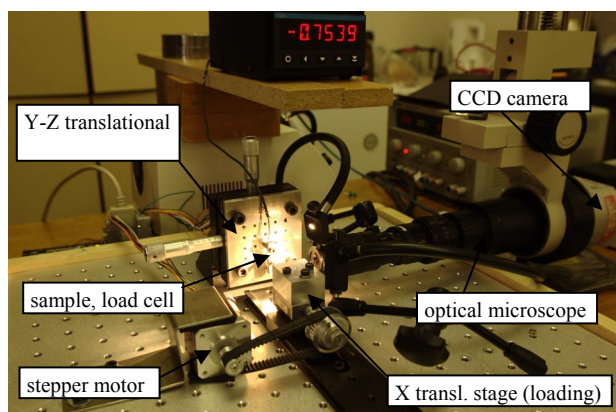


Fig. 2. Experimental setup for single trabecula tension tests

Due to the low value of Young's modulus of elasticity of the glue, the strain could not be calculated from the displacements of the end plates. Instead, the strain at the surface of the trabecula was calculated from the sequence of captured images using an image correlation algorithm<sup>5</sup>.

Prior the experiment, every sample was captured in two perpendicular projections along its longitudinal axis. The projections were used to generate a finite element (FE) model of each sample. The cross-section of the trabecula was approximated by ellipse with known dimensions of the main axes. These dimensions were calculated from the images taken prior the experiment.

The experiment consisted of 10 cycles of preconditioning immediately followed by tension up to the rupture. The preconditioning was performed to verify the boundary conditions, namely perfect setting of the glue. The preconditioning was controlled by a small displacement value not exceeding the elasticity limit. During the first 10 cycles the force was carefully controlled whether the values for the upper and lower limit is reached in every cycle. If there was change of the measured force exceeding 5 % of the original value during the first 10 cycles, the experiment was considered invalid and the results were excluded.

After successful preconditioning the sample was loaded up to the rupture and the force and sequence of captured images were recorded to the PC.

Total number of samples harvested from the block of trabecular bone was 28. From these 28 samples, 5 samples were damaged or lost during manipulation. From the remaining 23 samples, 7 samples were excluded due to insufficient curing of the glue. Two more samples were excluded due to excessive bending of the sample caused by its inappropriate (highly curved) geometry. Remaining 16 samples were successfully tested in tension and a stress-strain curve for each of the sample was obtained.

#### Nanoindentation

A small cubic sample of bone tissue was cut from the same anatomical place of the same donor using a diamond blade saw (Isomet 2100, Buehler Ltd., USA). The fat and marrow was removed from the sample using a soft water jet followed by repetitive ultrasonic cleaning. The sample was

fixed in low shrinkage epoxy resin (EpoxyCure, Buhler Ltd., USA), polished with diamond discs with grain size 35 and 15  $\mu\text{m}$  followed by monocrystalline diamond suspension with grain size 9, 3 and 1  $\mu\text{m}$ . For the final polishing aluminium-oxide  $\text{Al}_2\text{O}_3$  suspension with grain size 0.05  $\mu\text{m}$  on a soft cloth was used. Prior the mechanical testing the surface roughness of the sample was measured in a confocal laser scanning microscope (Lext OLS3000, Olympus America Inc., USA). The peak roughness  $R_p$  (the highest peak in the roughness profile) of the finished surface was 15 nm.

The sample was then fixed in nanoindenter Nanohardness tester (CSM Instruments, Switzerland) and indented using two different peak forces, 10 mN and 20 mN. For both peak forces a grid of 20 indents was performed with different set of parameters. Apart from the two peak forces, three different loading rates were used (20, 120, 240  $\text{mN min}^{-1}$ ) and three different holding times (10, 20, 40 s).

For each indent force-depth curves were plotted and hardness and modulus of elasticity were calculated using the Oliver-Pharr method<sup>6</sup>. Results from indents accidentally placed at the interface between two lamellae were excluded. At average, there were 16.75 successful indents in each set of parameters.

### 3. Results

From the 16 successfully performed tension tests with isolated trabeculae the strain values were evaluated using DIC method applied to two distant regions. The places for the image correlation were selected using approximately 4/5 of the free length of the sample as the gauge length. The measured force was divided by the cross-sectional area of the sample at the place of the rupture. The area was measured using 10 Mpx camera picture of the imprint of the broken sample. The broken torso of the sample was pressed into a surface of very soft material (modelling clay) to obtain the cross-sectional area. Example of the stress-strain diagram obtained from the tension test is presented in Fig. 4.

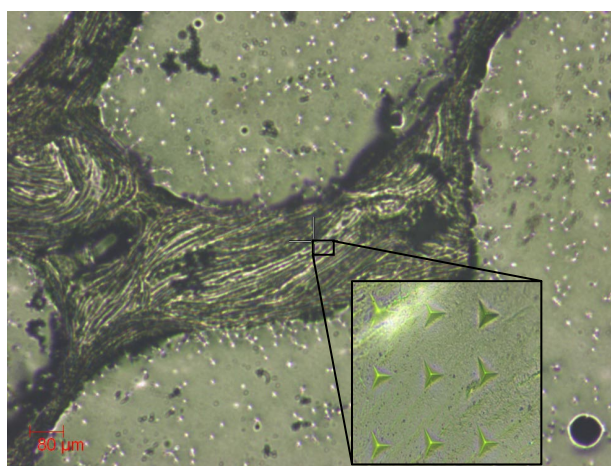


Fig. 3. Sample trabecula in light microscope showing a grid of indents

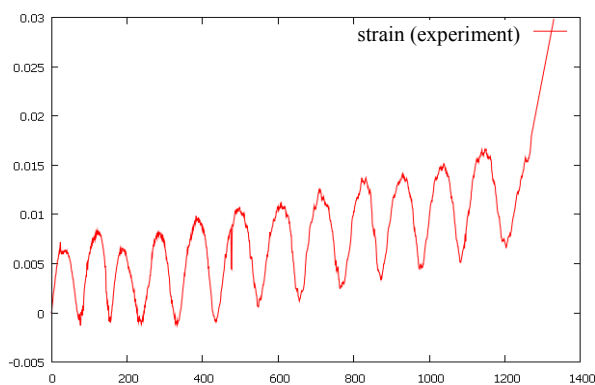


Fig. 4. Strain assessed using the DIC method (experiment)

## FE simulation of nanoindentation test

For FE simulations of the nanoindentation test a rotationally axisymmetric plane model was used. The Berkovich pyramid indenter was replaced with equivalent cone. The sharp tip of the cone was rounded due to the use of nonlinear contact between indenter and specimen. For the diamond nanoindenter elastic material model ( $E=1140$  GPa,  $\mu=0.04$ ) was used. The elasto-plastic model with von Mises yield criterion and bilinear isotropic hardening was chosen for trabecular bone. This material model is described by four material constants, Young modulus  $E$ , Poisson's ratio  $\mu$ , yield stress  $\sigma_y$  and tangent modulus  $E_{tan}$ . Young's modulus and Poisson's

Table I  
Identified material constants for 8 nanoindentation curves

$\sigma_y = 100.5$ MPa, $E_{tan} = 898$ MPa					
curve #	$E$ [GPa]	$\mu$	loading rate [mN min <sup>-1</sup> ]	max force [mN]	error
1	15.153	0.2	10	240	5716
2	13.959	0.2	10	240	2757
3	16.26	0.2	10	20	722
4	14.849	0.2	10	20	1446
5	17.543	0.2	10	20	2803
6	15.7	0.2	10	120	1945
7	18.482	0.2	20	20	1473
8	18.144	0.2	20	120	2274

$$error = \frac{\sum_{i=1}^n (u_i^{exp} - u_i^{fem})^2}{n}$$

$u_i^{exp}$  ..penetration depth in experiment (nm)

$u_i^{fem}$  .. penetration depth in FE simulation (nm)

$n$  ... number of approximations points

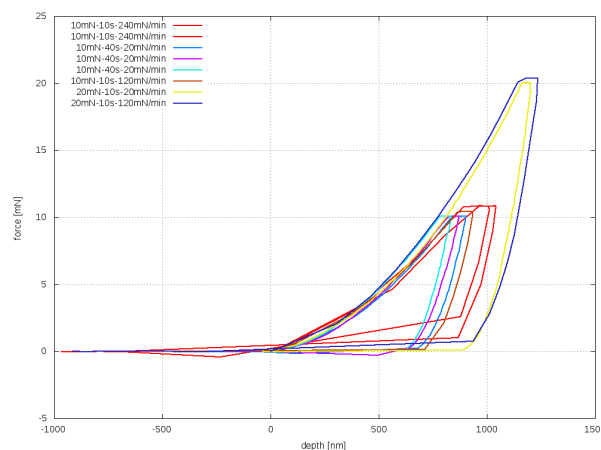


Fig. 5. Set of depth-force curves obtained by inverse FE modelling for eight selected sets of nanoindentation experiments

ratio were assumed to be the same as in the nanoindentation experiment. Remaining material constants ( $\sigma_y$ ,  $E_{tan}$ ) were evaluated by fitting the nanoindentation curves.

The set of nanoindentation curves with different load speeds, holding times and maximal forces was sampled using linear approximation. Values of force and penetration depth at approximation points were obtained from each nanoindentation curve. The force values with constant increments were prescribed to the model of indenter in each load step of the FE simulation (450 load steps per simulation). Nanoindentation curves obtained from the FE simulation were compared with experimental curves by the least squares method.

Material model identified by the above described fitting procedure was used in FE simulation of the single trabecula tension test. The geometry of the trabecula was approximated using elliptical cross-sections. The lengths of the major and minor axes of the ellipses were estimated from two projections of each trabecula captured by the CCD camera. The volume was discretized by 10-node tetrahedral elements with quadratic shape functions. The model was equipped with the bilinear isotropic hardening model identified from the nanoindentation. The loading was controlled by displacements according to the performed experiments. Obtained relationships between applied displacement and reaction force were compared with results obtained experimentally using the tension tests in terms of the stress-strain diagrams.

## 4. Conclusions

Comparison of material properties of human trabecular bone assessed by nanoindentation and tension tests performed on isolated trabeculae was performed. The elasto-plastic material model identified in the FE simulation of nanoindentation test was used in the numerical simulations of the tensile experiments. Obtained response of the FE model was compared with experimentally assessed stress-strain diagrams of the tested samples.

Resulting elastic modulus obtained from nanoindentation ( $E=16,34\pm1,76$  GPa) and from uniaxial testing ( $E=9,21\pm1,26$  GPa) gives mean values which differ signifi-

cantly, though the standard deviations are small. This might be caused by extremely irregular shape of tested tensile specimens, and we conclude that the source of error is imprecise calculation (overestimation) of the cross-sectional area of the samples. From the tensile tests of single trabeculae it was also possible to determine the yield stress ( $\sigma_y=176\pm 23$  MPa) and yield strain ( $2,85\pm 0,84$  %). However, these values cannot be directly compared to nanoindentation.

In this study, dry samples were used due to the difficulties connected to nanoindentation under wet conditions. For the tension tests it is possible to soak the samples in physiological solution prior the experiment (time needed for the experiment is sufficiently short), but it is still a challenge to perform the nanoindentation with wet samples. Performing the described experiments under wet conditions is the aim of our future research.

*The research has been supported by the Grant Agency of the Czech Republic (grant No. P105/10/2305), Ministry of Education of the Czech Republic (Research Plan MSM 6840770003) and research plan of the Academy of Sciences of the Czech Republic AV0Z20710524.*

#### REFERENCES

1. Verhulst E., van Rietbergen B., Müller R., Huiskes R.: J. Biomech. 41, 1479 (2008).
2. Jiroušek O., Jandajsek I., Vavřík D.: J. Inst. 6 (2011), C01039.
3. Rho J.-Y., Tsui T. Y., Pharr G. M.: Biomaterials 18, 1325 (1997).
4. Wolfram U., Wilke H.-J., Zysset P. K.: J. Biomech. 43, 1731 (2010).
5. Lucas B. D., Kanade T.: Proc. Im. Underst. Wshp 121 (1981).
6. Dendorfer S., Maier H. J., Hammer J.: J. Mech. Behavior Biomed. Mater. 2, 113 (2009).
7. Oliver W. C., Pharr G. M.: J. Mater. Res. 7, 1564 (1992).

**O. Jiroušek<sup>a</sup>, J. Němeček<sup>b</sup>, D. Kytýř<sup>a</sup>, J. Kunecký<sup>a</sup>, P. Zlámal<sup>a</sup>, and T. Doktor<sup>a</sup>** (<sup>a</sup>*Institute of Theoretical and Applied Mechanics, Academy of Sciences of the Czech Republic, Prague,* <sup>b</sup>*Czech Technical University in Prague, Faculty of Civil Engineering, Prague, Czech Republic*): **Nanoindentation of Trabecular Bone – Comparison with Uniaxial Testing of Single Trabecula**

To improve the knowledge about the mechanical properties of trabecular bone and their relationship with the properties of their constituting materials it is necessary to measure the properties at micrometer scale. The published mechanical properties of human trabecular bone vary between 1 GPa and 15 GPa. The cause of this broad discrepancy in results might be in sample preparation, different testing protocols or anisotropy and asymmetry of the micro-samples.

The article deals with a comparison between the properties assessed using nanoindentation and properties measured using uniaxial testing of single trabeculae.

A novel experimental device has been developed which enables to measure single trabeculae in tension and compression with high precision. The strains at the surface of the sample are measured optically using a high-resolution CCD camera. The strain field is evaluated with very precise image correlation algorithm applied to whole surface of the loaded sample.

The mechanical properties measured on micrometer-sized specimens using both methods (nanoindentation and micro-mechanical testing) are then prescribed to FE model of the trabecula sample. The sample is then loaded according to the experimental procedure. The response of the FE model (stress-strain curve) is compared to results from the tensile test.



# MICROMECHANICAL PROPERTIES OF POROUS MATERIAL BASED ON METAL FOAM

**VLASTIMIL KRÁLÍK\* and JIŘÍ NĚMEČEK**

Czech Technical University in Prague, Thákurova 7, 166 29  
Prague 6, Czech Republic  
vlastimil.kralik@fsv.cvut.cz

Keywords: Metal foam, Porous system, Nanoindentation, Micromechanical properties, Elastic properties, Deconvolution

## 1. Introduction

Traditionally, materials were tested on large samples by macroscopic methods that can give overall (or effective) properties. Together with the development of experimental techniques in the past, microstructural and micromechanical properties have become important in the description of the material behavior since they could give answers on the origin of many macrolevel phenomena.

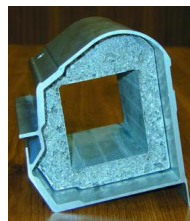
Structural materials (like cement, lime or gypsum composites as well as metals, wood or plastic) often exhibit large variation in the microstructure of their solid phases. They are also often characterized by a closed or open pore system. Porosity is usually smaller than the solid phase content but the situation is opposite in case of lightweight materials. An exceptional example is metal foam which typically exhibits porosity around 90 % of the sample volume. Its cellular structure is analogous to the natural materials like wood or bones. Metal foams belong to the up-to-date structural materials with high potential to many engineering applications. This highly porous material with a cellular structure is known for its attractive mechanical and physical characteristics such as high stiffness in conjunction with very low weight, high strength, excellent impact energy absorption, high damping capacity and good sound absorption capability.

The usual source material for the production of metal foams is aluminium and aluminium alloys because of low specific density ( $\sim 2700 \text{ kg m}^{-3}$ ), low melting point ( $\sim 660^\circ\text{C}$ ), nonflammability, possibility of recycling and excellent corrosion resistivity.

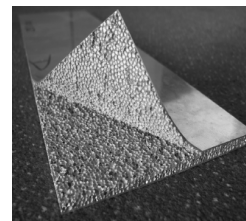
Products of aluminium foams gained a growing research interest in many engineering branches. They are used in applications ranging from automotive and aerospace industries (Fig. 1) to building industry (e.g. sound proofing panels). Another application of aluminium foams can be found in energy absorption (e.g. the outer shell of motorcycle helmets). More structural and functional applications of metal foams for industrial sectors have been reviewed e.g. by Banhart<sup>1</sup>.

Metal foam can be described as a system with stochastically distributed solid phase which in turn brings difficulties in the modeling of different loading cases.

In general, mechanical properties of metal foams are governed by two major factors: (i) cell morphology (shape,



a



b

Fig. 1. Examples of aluminium foam components. (a) Reinforcement of car body sill, (b) sandwich panel

size and distribution of cells) and (ii) material properties of the cell walls<sup>2</sup>. However, measurement of mechanical properties of the cell walls is a difficult problem that cannot be solved with conventional methods due to their small dimensions, low local bearing capacity and local yielding and bending of the cell walls. These problems can be overcome using micromechanical methods in which the load–displacement curve is obtained in the sub-micrometer range.

In this study, nanoindentation was applied to access elastic properties of the distinct phases within the cell walls of a conventional metal foam system.

## 2. Materials and methods

### 2.1. Tested material

Commercial aluminium foam ‘Alporas’ (Shinko Wire Co., Ltd) was tested in this study. Alporas is an ultra-light weight material with a closed cell structure. The manufacturing process of the Alporas is a batch casting process<sup>3</sup> in which 1.5 wt.% of calcium is added to the aluminium molten at  $680^\circ\text{C}$ . Calcium serves as a thickening agent which increases viscosity and stabilizes the air bubbles. The alloy is poured into a casting mold and stirred with an admixture of 1.6 wt.%  $\text{TiH}_2$  that is used as a blowing agent. Then, the foamed molten material is cooled down. A typical resulting internal structure of the aluminium foam is shown in Fig. 2.

### 2.2. Specimen preparation

Small Alporas block  $14 \times 14 \times 43 \text{ mm}$  was firstly embedded into cylindrical mould (30 mm in diameter, 60 mm in height) which was filled with a low viscosity epoxy resin (Struers<sup>®</sup>). Then,  $\sim 5 \text{ mm}$  slices were cut by diamond saw and polished with fine SiC papers. Resulting surface roughness was checked with *in-situ* imaging (surface scanning was performed with the same tip as for nanoindentation). Several roughness criteria were used (ref.<sup>4</sup>). For example, arithmetic deviation from the mean is defined as:

$$R_a = \frac{1}{M \cdot N} \sum_{i=1}^M \sum_{j=1}^N |h_{ij} - \bar{h}|$$

or quadratic deviation (root-mean-square):

$$R_q = \sqrt{\frac{1}{M \cdot N} \sum_{i=1}^M \sum_{j=1}^N |h_{ij} - \bar{h}|^2}$$

In the above equations,  $M$  and  $N$  are numbers of the measured points in two perpendicular directions with heights  $h_{ij}$  ( $i=1..N$ ;  $j=1..M$ ) and  $\bar{h}$  is the arithmetic mean from all measured surface heights.

As a rule of thumb, the surface roughness should be kept within 10% of the expected maximum depths used in nanoindentation. In our case,  $R_a \approx 24$  nm and  $R_q \approx 30$  nm were found on a  $20 \times 20$   $\mu\text{m}$  scan (Fig. 3) which was acceptable compared to the maximum indentation depths around 300 nm.

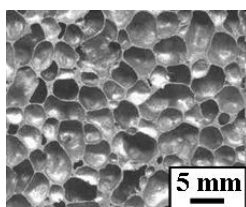


Fig. 2. Typical structure of aluminium foam 'Alporas'

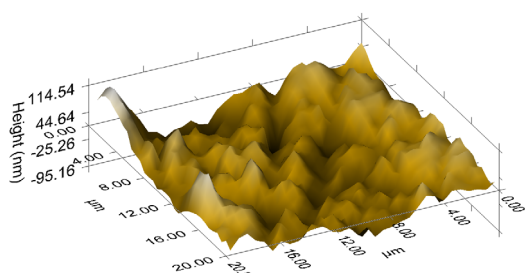


Fig. 3. 3D map of the sample surface on  $20 \times 20$   $\mu\text{m}$  area

### 2.3. ESEM and porosity

The microstructure of the foam was studied in electron microscope (ESEM). The non-homogeneous solid phase of the cell wall is shown in Fig. 4. Two distinct phases, that exhibit different color in back-scattered electron (BSE) images, can be distinguished. The chemical composition of the two phases was checked with EDX element analysis in ESEM. It was found that the majority of the volume (dark zone) consists of aluminium (~67 wt.%), oxygen (~32 wt.%) and further trace elements (Mg, Ti, Fe, Co, Ni, Cu, Si <2 wt.%).

Lighter zones in Fig. 4 consist of Al (~60 wt.%), O (~30 wt.%), Ca (~5 wt.%), Ti (~5 wt.%) and other elements (<1 wt.%). As expected, the majority of the volume (dark zone) is composed of aluminium and aluminium oxide  $\text{Al}_2\text{O}_3$  (further denoted as Al-rich area). Lighter zones contain significant amount of calcium and titanium (further denoted as Ti-rich area). The non-uniform distribution of these zones shows on inhomogeneous mixing of the admixtures that are added during the production process.

The overall porosity of the sample reaches 90 % (ref.<sup>3</sup>). The large pores have usually round of polyhedral shape with the mean size 4,8 mm (ref.<sup>3</sup>). It can be seen in Fig. 4 that also a smaller part of porosity takes place on microlevel in a micron to submicron range. Further quantification of this 'small' porosity was beyond the scope of this study but it is planned in a near future.

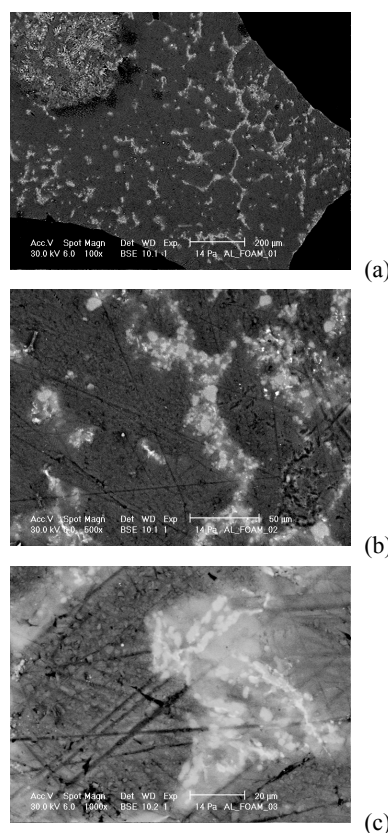


Fig. 4. ESEM Images of a cell wall: (a) overall view, (b) and (c) details of Ca/Ti-rich area (light zones)

### 2.4. Nanoindentation

The nanoindentation testing was performed using a Hysitron Tribolab system<sup>®</sup> at the CTU in Prague. This system consists of *in-situ* SPM imaging which was used for scanning the sample surface. Berkovich tip was used for all measurements. Five distant locations were chosen on the sample to capture its heterogeneity. Each location was covered by a series of  $10 \times 10$  indents with 10  $\mu\text{m}$  spacing (Fig. 5). It yields 500 indents in total which was considered to give suffi-

ciently large statistical set of data. Standard load controlled test of an individual indent consisted of three segments: loading, holding at the peak and unloading. Loading and unloading of this trapezoidal loading function lasted for 5 second, the holding part lasted for 10 seconds. Maximum applied load was 1500  $\mu\text{N}$ .

Elastic constants (hardness and elastic modulus) were evaluated with standard Oliver and Pharr method<sup>5</sup>. Poisson's ratio needed for the estimation of Young's modulus was chosen to be 0,35 for all indents (equivalent to Aluminium<sup>6</sup>).

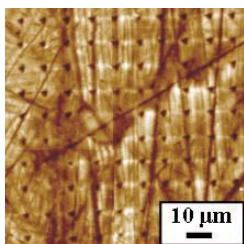


Fig. 5. Matrix of 10×10 indents scanned with Hysitron Tribolab®

### 3. Results

#### 3.1. Statistical results from nanoindentation

An example of a typical loading diagram for Al-rich area (dark zone in Fig. 4) is shown in Fig. 6a. Average contact depth is around 230 nm and maximum depth reaches values around 240 nm. The material volume affected by nanoindentation can be estimated as 3 to 4 times the maximum depth, i.e. < 1  $\mu\text{m}$  (ref.<sup>8</sup>). Variety of results from different positions is shown in Fig. 6b in which a part of curves belongs to Al-rich and a part to Ca/Ti-rich zones.

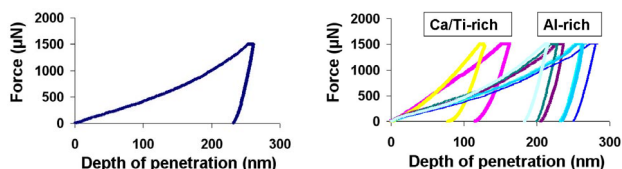


Fig. 6. (a) Typical loading diagram for Al-rich zone, (b) example of variation in loading diagrams for Ca/Ti-rich zone

The scatter in the results is affected mainly by the position in different zones and related hardnesses of its constituents. On the other hand, absolute values of elastic constants are affected also by a porosity which is expected to be close to the maximum indentation depth. The porosity is naturally included in the results that are measured for a solid volume consisting this part of the porosity. Overall results are depicted in Fig. 7 in which histogram of all elastic moduli merged from all positions is shown.

It can be seen in Fig. 7 that a significant peak appears around 40 GPa. This value can be considered as a dominant characteristic of a solid phase. More detailed specification is given in the next section. Large scatter in the results can be attributed to the heterogeneous chemical and mechanical

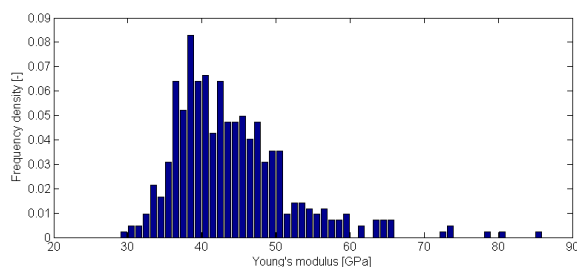


Fig. 7. Histogram of elastic moduli merged from all positions

composition (e.g. addition of Ca and Ti) in the sample and also to the porosity as discussed before.

Average mechanical results from all measurements are summarized in the Tab. I.

Evaluated average Young's modulus  $E$  lies between 40 to 51 GPa for individual locations. These values and also the dominant characteristic from Fig. 7 (~40 GPa) are much lower than that for pure aluminium (70 GPa, ref.<sup>6</sup>) which is another evidence of the sample heterogeneity and introduced micro porosity. Youngs' moduli of calcium (20 GPa, ref.<sup>6</sup>) and titanium (116 GPa, ref.<sup>6</sup>) are also far from the mean value of  $E$  and cannot be found in the overall histogram (Fig. 7) either. It shows on their mechanical interaction within the scale of the nanoindentation. Perhaps, their properties are included in one effective phase (Ca/Ti-rich).

Table I

Average values of micromechanical parameters

Position	Number of indents	Young's modulus [GPa]	St. dev. [GPa]	Hardness [GPa]	St. dev. [GPa]
1	100	43,4	8,69	0,929	0,524
2	100	40,7	4,48	0,737	0,137
3	100	41,2	6,32	0,734	0,099
4	100	51,2	9,21	1,090	0,453
5	100	46,9	7,37	0,941	0,240

#### 3.2. Deconvolution

Statistical results of elastic moduli (Fig. 7) have been further analyzed with a deconvolution technique<sup>7–9</sup> which seeks for parameters of individual phases included in overall results. The deconvolution algorithm searches for  $n$ -Gauss distributions in an experimental probability density function – PDF (Fig. 7). Random seed and minimizing criteria of the differences between the experimental and theoretical overall PDFs are computed in the algorithm to find the best fit.

Tab. II contains numerical results from the deconvolution also with the estimated volume fractions of the phases. Two-phase system (one dominant Al-rich phase and one minor Ca/Ti-rich phase) was assumed in the deconvolution.

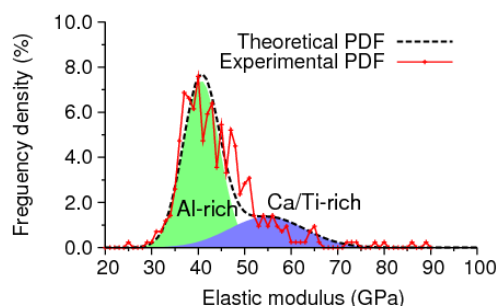


Fig. 8. Comparison of the experimental probability density function with the results from deconvolution in two phases

Table II  
Elastic moduli (GPa) from deconvolution

Phase	Mean	St. dev.	Volume fraction
1 (Al-rich zone)	40,67	3,93	0,723
2 (Ca/Ti-rich zone)	54,80	8,08	0,277

#### 4. Conclusions

Performed microstructural observations and results from nanoindentation revealed that the heterogeneity included in the aluminium foam at the production process has consequences in its micromechanical behavior. Large scatter of elastic parameters have been obtained. Harder and softer areas measured with nanoindentation can be linked with ESEM analyses and denoted as Al- and Ca/Ti-rich areas. Average mechanical results of a dominant Al-rich phase (40,67 GPa) do not reach values expected for a pure aluminium (~70 GPa). It points out to the fact that a substantial part of the sample porosity can be included in the tested volume (~1  $\mu\text{m}$ ) and/or softer admixtures influence on the obtained results.

Further research on the microporosity, influence of admixtures and also measurement of inelastic properties is planned in the future. Results should serve as an input data for mathematical modeling of the material.

Support of the Czech Science Foundation (GAČR 103/09/1748) and Agency of the Czech Technical University in Prague, grant No. SGS10/135/OHK1/2T/11, is gratefully acknowledged.

#### REFERENCES

1. Banhart J.: *Progr. Mater. Sci.* 46, 559 (2001).
2. Hasan M. A., Kim A., Lee H.-J.: *Compos. Structur.* 83, 180 (2008).
3. Miyoshi T., Itoh M., Akiyama S., Kitahara A., Aluminium foam, "ALPORAS": *Mat. Res. Soc. Symp. Proc.*, Vol. 521, Materials Research Society 1998.
4. ISO 4287-1997, "Geometrical Product Specifications (GPS) – Surface texture: Profile method – Terms, definitions and surface texture parameters"
5. Oliver W., Pharr G.: *J. Mater. Res.* 7 (1992).
6. WebElements Periodic Table of the Elements. <http://www.webelements.com>
7. Constantinides G., Chandran K. R., Ulm F.-J., Vliet K. V.: *J. Mater. Sci. Eng., A* 430 (2006).
8. Němeček J., Lukeš J.: *Chem. Listy* 104, s279 (2010).
9. Němeček J., Šmilauer V., Kopecký L., accepted for publication in *Cem. & Concr. Comp.*, ISSN: 0958-9465.

V. Králík, and J. Němeček (*Czech Technical University in Prague*): **Micromechanical Properties of Porous Material Based on Metal Foam**

This paper deals with the study of microstructure and micromechanical properties of a porous aluminium-based material using nanoindentation. ESEM analysis revealed Al- and Ca/Ti-rich areas. Results of elastic moduli and hardness monitored in five distant locations on the solid pore walls. On a large statistical set of measurements analysed using deconvolution method indicated, that average elastic modulus of dominant Al-rich phase is 40.67 GPa and minor Ca/Ti-rich phase 54.80. They are lower than the values for pure aluminium (~70 GPa), possibly due to additional microporosity.



# IDENTIFICATION OF STRESS-STRAIN RELATION OF AUSTENITIC STEELS BY INSTRUMENTED INDENTATION

**PETR HAUSILD<sup>a\*</sup>, JIŘÍ NOHAVA<sup>b</sup>,  
and ALEŠ MATERNA<sup>a</sup>**

<sup>a</sup> Czech Technical University in Prague, Faculty of Nuclear Sciences and Physical Engineering, Department of Materials, Trojanova 13, 120 00 Praha, Czech Republic, <sup>b</sup> CSM Instruments, Rue de la Gare 4, CH-2034 Peseux, Switzerland  
hausild@fffi.cvut.cz

Keywords: Nanoindentation; Stainless steel; Martensitic transformation; Finite element method

## 1. Introduction

Instrumented indentation with spherical indenter is extensively used for characterization of local mechanical properties of various materials including metals, ceramics and polymers. For elastic-plastic behavior of metals, definitions of indentation stress and representative strain proposed by Tabor<sup>1</sup> are widely accepted and have since been verified by other investigators<sup>2–4</sup>.

Indentation (or representative) stress is given by:

$$\sigma_{repr} = \frac{P}{C \pi a^2} \quad (1)$$

where  $P$  is the load,  $a$  is the indentation radius (see Fig. 1) and  $C$  is the constraint factor about 3 for most perfectly plastic engineering materials.

Representative (or average) strain is given by:

$$\varepsilon_{repr} = 0.2 \frac{a}{R} \quad (2)$$

where  $R$  is the radius of the spherical indenter, prefactor 0.2 was determined empirically<sup>1</sup>.

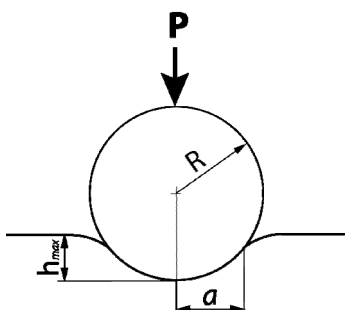


Fig. 1. Schematic diagram of an indentation by a rigid sphere

The main assumption of this approach is that the indentation (compressive) stress and strain are similar to their counterparts in uniaxial loading, i.e.:

$$\sigma_{repr} = \sigma_{uniaxial} \quad \text{and} \quad \varepsilon_{repr} = \varepsilon_{uniaxial} \quad (3)$$

In this paper, the local stress-strain relations of two common austenitic stainless steels (grade A301 and A304) are characterized by instrumented indentation with spherical indenter. The results obtained by indentation are compared with tensile stress-strain curves and analyzed using finite element model. The limitations of such identified relations arise from the indenter shape, uneven contact and non-linear material behavior due to e.g. cracking or phase transformation. Especially AISI 301 steel undergoes at room temperature deformation-induced phase transformation of face-centered cubic  $\gamma$  austenite to body-centered cubic  $\alpha'$ -martensite<sup>5</sup>. High internal stresses are generated due to an incompatible transformation strain accompanying the martensitic transformation<sup>6</sup>. The correct interpretation of the measured local properties is therefore essential for good understanding of the material behavior of metastable austenitic steels subjected to plastic strain.

## 2. Experimental details

Two austenitic stainless steels (AISI 301 and 304) were chosen as an experimental material. The chemical composition is given in Tab. I. The steels were supplied by the ARCELOR-MITTAL as cold rolled sheets (thickness 0.68 mm and 0.8 mm respectively) in the annealed state. Surface of samples was electro-polished in 5 % perchloric acid solution in ethanol at 40 V to avoid the surface layer affected by mechanical grinding and polishing.

Nanoindentation measurements were performed on CSM Instruments NHT Nanoindentation Tester with spherical indenter using instrumented indentation technique. A small indenter radius (5  $\mu\text{m}$ ) was chosen to achieve fully plastic deformation under the indent. Single indentation and continuous multi cycle (CMC) indentation with increasing load were performed up to maximum load of 100 mN. Loading time was 10 s per each cycle for CMC, followed by 5 s hold at the maximum load and unloading time 10 s per each cycle. For single indentation, both loading and unloading times were set to 30 s while the hold period at the maximum load was maintained at 5 s.

Table I  
Chemical composition of stainless steels (in wt.%)

	C	Cr	Ni	Si	Mn	Mo
A301	0.05	17	7	0.5	1.5	0.1
A304	0.04	18.3	9.2	0.5	1.5	0.18

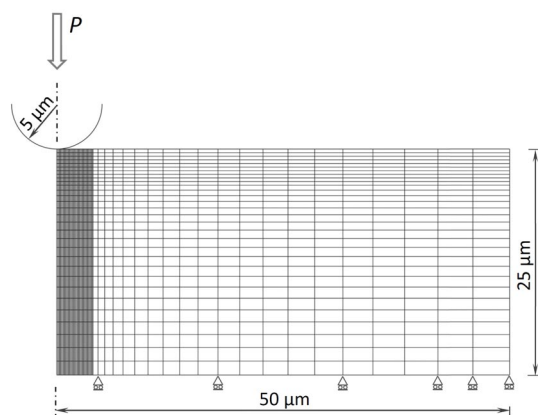


Fig. 2. Finite element mesh and boundary conditions used for the simulation of indentation experiment

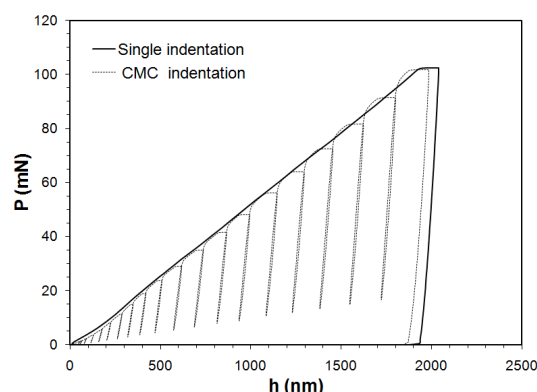


Fig. 3. Typical single and CMC indentation load vs indentation depth curve obtained on A304 stainless steels

### 3. Finite element modelling

A forward analysis of Tabor's relations was carried out using finite element method (FEM). FEM model was implemented in Msc.Marc 2010 FEM code. The specimen was modelled by 4000 8-node quadratic axisymmetric elements with the finest mesh (mesh size  $100 \times 400$  nm) in the region of the indented material (Fig. 2). The indenter was modelled by a rigid contact surface. Elasticity in the indenter was neglected since it is important only for very hard materials (comparable to diamond). The plastic response of the material was governed by von Mises (J2) yield criterion, associated flow rule, isotropic hardening and the constitutive responses obtained from the tensile tests.

### 4. Results and discussion

Typical load versus indentation depth plot is shown in Fig. 3. Single indentation and continuous multi cycle (CMC) indentation records obtained on both stainless steels are in very good agreement which justifies using indentation stress and indentation radius measured by CMC indentation for the representative stress-representative strain evaluation.

The global responses computed by FEM are compared with the experimental load versus indentation depth curves in Fig. 4. For both steels, the simulated loading parts are in a good agreement with the experimental curves (keep in mind that viscous effects during hold and unload were not considered in FEM modelling).

The small differences between the experimental and simulated loading curve in the case of A301 steel are caused by the transformation induced plasticity which is not taken into account in the modeled material behavior.

Martensitic transformation is a first order phase transformation (accompanied by the volume change).

In the case of intervening such phase transformation, the actual macroscopic (mean) inelastic strain rate,  $\bar{\epsilon}_{pl}$ , is given by:

$$\bar{\epsilon}_{pl} = (1 - f_m) \bar{\epsilon}_{pa} + f_m \bar{\epsilon}_{pm} + f_m \bar{\epsilon}_{tr} \quad (4)$$

i.e., consists of the plastic deformation in the austenite  $\epsilon_{pa}$ , martensite  $\epsilon_{pm}$ , and the transformation induced plasticity  $\epsilon_{tr}$  ( $f_m$  is the martensitic volume fraction).

The modeled distributions of equivalent plastic strain (at the maximum load) are shown in Fig. 5 and 6 respectively. There is a higher gradient of equivalent plastic strain under the indenter in the A304 steel due to the different plastic response. It is also interesting to note the maximum value of equivalent plastic strain ( $\epsilon_{pl} \sim 0.7$ ) in comparison with representative (mean) strain ( $\epsilon_{repr} \sim 0.15$ ) obtained from eq. (2).

Stress-strain relations obtained using Tabor's formula from nanoindentation experiment are compared with tensile test and FEM modeling in Fig. 7.

In the case of A304 steel, there is almost a perfect fit of tensile curve after some initial stage. The discrepancy for small representative strains (low indentation depths and small

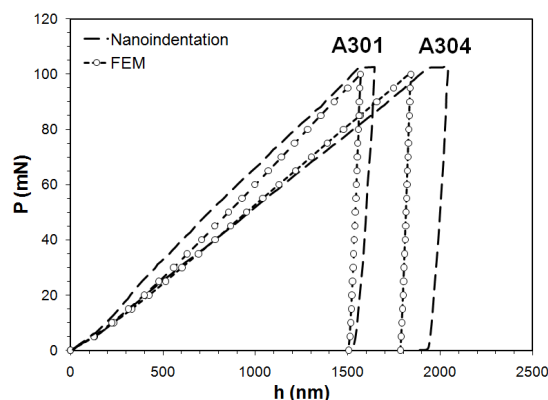


Fig. 4. Experimental and simulated (FEM) load vs indentation depth curves obtained by single indentation with spherical indenter

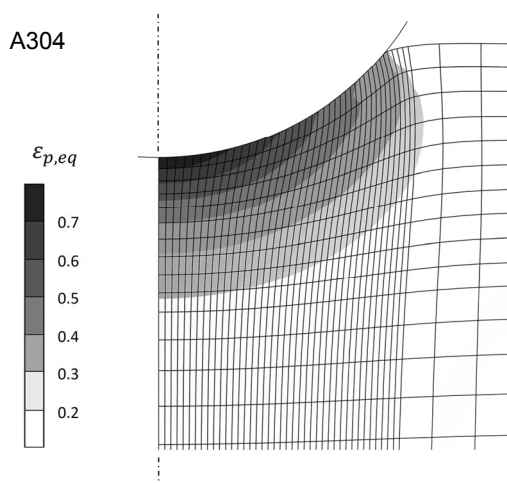


Fig. 5. Equivalent plastic strain distribution under the indenter in A304 steel computed by FEM model ( $P=100$  mN,  $\varepsilon_{repr}=0.15$ )

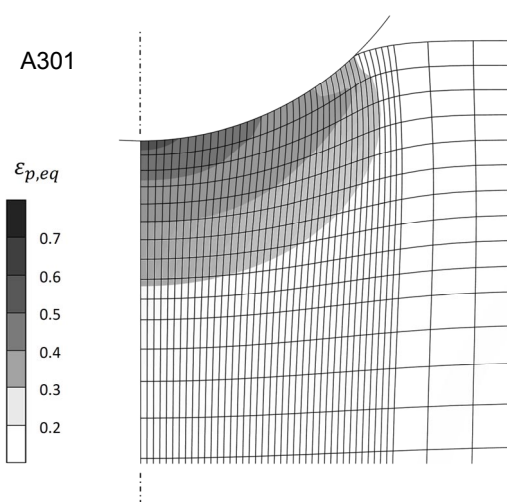


Fig. 6. Equivalent plastic strain distribution under the indenter in A301 steel computed by FEM model ( $P=100$  mN,  $\varepsilon_{repr}=0.14$ )

indentation areas) is probably caused by imperfect (worn) indenter radius and/or surface roughness (see Fig. 8b). This could partially be resolved by using larger indenter radius (keeping the low indentation depths but increasing the indentation contact areas) but care must be taken to remain in plastically dominated regime.

In the case of A301 steel, the non-linear material behavior caused by the deformation induced martensitic transformation resulted in a large discrepancy between indentation and tensile test data within the whole interval of interest. In this case, a reverse analysis with much complex materials constitutive behavior must be employed to identify the stress-strain relations.

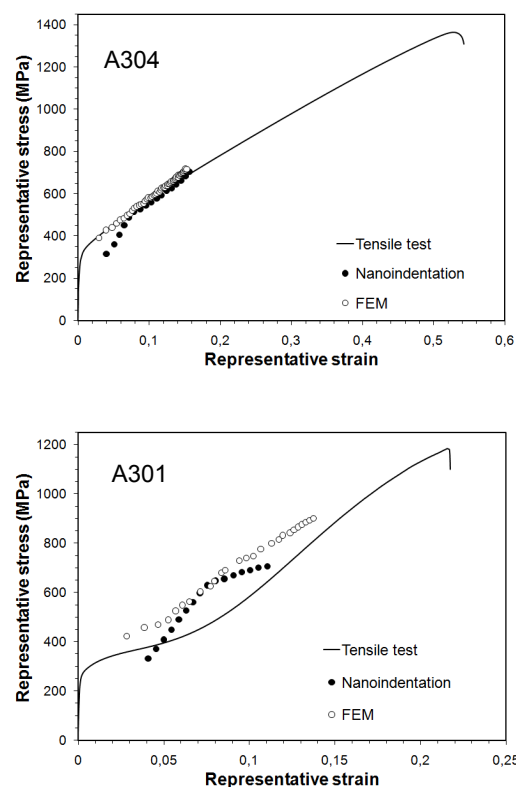


Fig. 7. Stress-strain relations obtained by tensile test, using Tabor's formula from nanoindentation experiment and FEM model

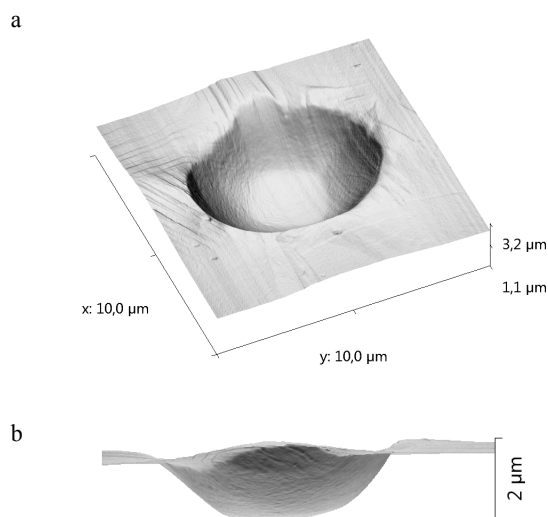


Fig. 8. Atomic force microscopy image of the indent by  $5\text{ }\mu\text{m}$ -radius indenter (a), side view (b). A301 steel,  $P=100$  mN

## 5. Conclusions

The instrumented indentation technique with a small indenter radius was successfully used for the prediction of the local mechanical behavior of stainless steels in the fully plastic regime.

Indentation experiments were modeled by FEM. FEM simulations reproduced properly the global response of the material to the spherical indentation and allowed us to assess the stress-strain distribution under the indent. FEM simulations showed also the limitations of the instrumented indentation method.

Finally, it must be pointed out that using of Tabor's formula without a full consideration of the character of the indentation process with respect to the elastic-plastic properties of the specimen material can lead to erroneous results especially in the case of intervening phase transformation.

*This work was carried out in the frame of research project GA CR 101/09/0702.*

## REFERENCES

1. Tabor D.: *The Hardness of Metals*, Clarendon Press, Oxford 1951.
2. Johnson K. L.: *Contact mechanics*. Cambridge University Press, 1985.

3. Fischer-Cripps A. C.: *J. Mater. Sci.* 32, 727 (1997).
4. Park Y. J., Pharr G. M.: *Thin Solid Films* 447-448, 246 (2004).
5. Magonon Jr., L., Thomas G.: *Metall. Trans. I*, 1577 (1970).
6. Timokhina I., Hodgson P., Pereloma E.: Effect of alloying elements on the microstructure-property relationship in thermomechanically processed C-Mn-Si TRIP steels. In: De Cooman BC, editor. *Proceedings of the international conference on TRIP-aided high strength ferrous alloys, Ghent*, 153–7, 2002.

**P. Haušild<sup>a</sup>, J. Nohava<sup>b</sup>, and A. Materna<sup>a</sup>,** (<sup>a</sup> Faculty of Nuclear Sciences and Physical Engineering, Czech Technical University in Prague, Czech Republic, <sup>b</sup> CSM Instruments, Switzerland): **Identification of Stress-Strain Relation of Austenitic Steels by Instrumented Indentation**

In this paper, the local stress-strain relations of two austenitic steels (grade A301 and A304) are characterized by instrumented indentation with spherical indenter. The results obtained by indentation are compared with tensile stress-strain curves and analyzed using finite element model. The limitations of such identified relations arising from the indenter shape, uneven contact and non-linear material behavior due to the stress-induced phase transformation are discussed.